Hierarchical porous iron and nitrogen co-doped carbons as efficient oxygen reduction electrocatalysts in neutral media

Yunhe Su, Hongliang Jiang, Yihua Zhu*, Wenjian Zou, Xiaoling Yang, Jianding Chen*, Chunzhong Li

Key Laboratory for Ultrafine Materials of Ministry of Education, School of Materials Science and Engineering, East China University of Science and Technology, 130 Meilong Road, Shanghai 200237, China

HIGHLIGHTS

- Hierarchical porous iron and nitrogen co-doped carbons have been successfully prepared.
- The synthesized HP−Fe−N−Cs show efficient ORR catalytic activities in neutral media.
- The HP−Fe−N−C-900 shows comparable MFCs performance to the commercial Pt/C catalyst.

GRAPHICAL ABSTRACT
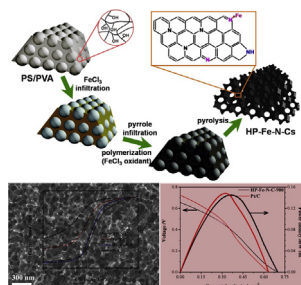
ABSTRACT

Hierarchical porous iron and nitrogen co-doped carbons (HP−Fe−N−Cs) as efficient cathode catalysts for oxygen reduction reaction (ORR) in neutral media are reported. The HP−Fe−N−Cs are prepared by using polypyrrole as nitrogen source and poly(vinyl alcohol) (PVA) hydrogel-based composites as in-situ templates. In studying the effect of the iron and the hierarchical porous structure on the nitrogen-doped carbon support for ORR, we find that HP−Fe−N−Cs show more positive onset potential, higher cathodic current density, and higher electron transfer number for the ORR in neutral media than iron-free hierarchical porous nitrogen-doped carbon (HP−N−C) and non-hierarchical porous iron and nitrogen co-doped carbon (Fe−N−C), highlighting the importance of the iron and the hierarchical porous structure for improving the ORR performance. Furthermore, HP−Fe−N−Cs show better durability than the commercial Pt/C catalysts in neutral media, and the microbial fuel cells (MFCs) equipped with HP−Fe−N−Cs catalysts on cathodes exhibit comparable power outputs with those of MFCs with commercial Pt/C cathode catalysts.

© 2014 Elsevier B.V. All rights reserved.

1. Introduction

The oxygen reduction reaction (ORR) on the cathode plays a key role in energy-conversion devices such as fuel cells (FCs) and metal−air batteries [1,2]. Pt and Pt based catalysts have long been regarded as the most efficient catalysts for ORR [3,4]. However, the issues of increasing scarcity, high cost and poor stability hinder Pt cathode application [5,6]. Therefore, developing sustainable Pt-free catalysts is essential for the commercialization of fuel cells and metal-air batteries technology [7,8].

Currently, heteroatom-doped carbon materials, especially N-doped carbon materials are demonstrated to be a new kind of

* Corresponding authors. Tel.: +86 21 64252022; fax: +86 21 64250624.
  E-mail addresses: yhzhu@ecust.edu.cn (Y. Zhu), jiandingchen@ecust.edu.cn (J. Chen).

promising non-Pt electrocatalyst for ORR [9–11]. The nitrogen doping in carbon materials can significantly enhance the number of active sites for improved ORR activity [12,13]. For instance, vertically aligned N-doped carbon nanotubes exhibit outstanding electrocatalytic activity, and better stability than 20 wt% Pt/C for ORR in alkaline media [9]. However, for most N-doped carbon materials, the ORR activities are still on a less competitive level compared to Pt catalysts. It is proposed that an important limitation for enhancing the catalytic activity of these systems is the low surface density of catalytic active sites [14,15]. In this regard, an effective solution is to synthesize electrocatalysts with high-surface-area and porous structure. The high-surface-area characteristic could increase the volumetric surface area and thus to improve the surface density of catalytic active sites, while the porous structure could improve the transport properties of ORR-relevant species (H^+, OH^-, e^-, O_2, H_2O) [12,16]. Unfortunately, this solution usually need some specific pore-forming templates such as colloidal silica and mesoporous silica SBA-15 to produce the porous structure and high-surface-area, which may result in relatively complicated preparation processes due to the etching treatment [14,17,18]. Another potential solution is to incorporate transition metals into nitrogen-doped carbon materials, which are commonly known as non-precious metal (NPM) catalysts [19]. The transition metals could not only promote the formation of graphitized carbon framework, but also be conducive to the formation of more catalytic active sites [20]. What's more, the intrinsic active sites of Me–N_x may also form between the transition metals and the doped nitrogen atoms, which could significantly improve the ORR activity of the transition metals based nitrogen-doped carbon materials [21,22].

Therefore, considering that both high-surface-area, porous structure and transition metals incorporation are in favor of promoting the ORR performance for catalysts, it would be encouraging and significant to synthesize porous NPM catalysts with high-surface-area and investigate their performances toward ORR. Just recently, some NPM catalysts with porous structure have been developed and demonstrated to show enhanced ORR activity and superior stability, including pyrolyzed Fe-polypyrrole mesoporous spheres, hierarchical interconnected macro-/mesoporous Co-containing N-doped carbon and mesoporous cobalt–nitrogen-doped carbon etc [15,23,24]. These studies indicate that hierarchical porous materials with interconnecting macro-/mesoporous structures are ideal ORR electrocatalysts, as they provide multidimensional electron transport pathways, large surface areas for reaction, interfacial transport, or dispersion of active sites at different length scales of pores, and shorter diffusion paths or reduce the diffusion effect [25]. However, despite tremendous progress in NPM catalysts for ORR, developing a convenient, economical, and scalable method to prepare NPM catalysts with hierarchical porous structure is still urgently required. Furthermore, to the best of our knowledge, there are no studies are devoted to investigating the ORR performances of hierarchical porous NPM catalysts in neutral solution and even their practical applications in biological systems.

In this article, a facile and simple strategy for preparing hierarchical porous iron and nitrogen co-doped carbons (HP–Fe–N–Cs) has been reported by using polypyrrole (PPy) as a nitrogen source and poly(vinyl alcohol) (PVA) hydrogel-based composites as in situ templates, which were prepared by the solvent-assisted freezethaw method we previously developed. The presence of PVA hydrogel endows the templates with the hydrophilic character and hydroxyls of PVA allow for easy adsorption of metal cations due to complexing action between hydroxyls and metal cations, which facilitate the infiltration process. Remarkably, the resulting HP–Fe–N–Cs possess high surface area, hierarchical porous structure, and a certain amount of possibly existed Fe–N_x moieties which could act as active sites in the ORR catalytic process. Consequently, the as-prepared HP–Fe–N–Cs display excellent electrocatalytic performance for a four-electron pathway ORR and long-term stability superior to the commercial Pt/C catalyst in neutral media. Moreover, the feasibility of HP–Fe–N–C composite as cathode catalyst in MFCs was also evaluated by comparing with the commercial Pt/C catalyst, which manifests a comparable performance to Pt/C.

2. Experimental section

2.1. Materials

Poly(vinyl alcohol) (PVA, 99% hydrolyzed, DP = 1750 ± 50) was purchased from Sinopharm Chemical Reagent Co. All other chemicals were purchased from Shanghai Lingfeng Chemical Reagent Co. Styrene (St) was purified by treatment with a 5% (w/w) aqueous NaOH solution to remove the inhibitor. Ultrapure water (18 MΩ cm) was used in all experiments.

2.2. Synthesis

PVA hydrogel-based composites templates were synthesized by the solvent-assisted freeze–thaw method we developed previously [26]. Typically, a 10% (w/w) PVA dimethyl sulfoxide (DMSO) solution was mixed with a 10% (w/w) latex (v/v = 1/1) of monodisperse polystyrene (PS) colloids with a diameter of 160 nm. Then the pregel solution gelled at −20 °C for 4 h, thawed at room temperature for 1 h, and then chemically cross-linked in 0.75% glutaraldehyde aqueous solution for 4 h to form PVA hydrogel-based composites. For the synthesis of hierarchical porous iron and nitrogen co-doped carbon materials (HP–Fe–N–Cs), 5 g of PVA hydrogel-based composites were pre-impregnated into 20 mL of 0.1 M $FeCl_3$ ethanol solution by stirring for 5 h at room temperature. Afterward, the PVA hydrogel-based composites were transferred into an ethanol solution (0.2 M) of pyrrole monomer and stirred for 30 min. Then, 30 mL of aqueous solution (0.1 M) of $FeCl_3$ was added to the suspension followed by stirring for 24 h at 4 °C. The resulting solid was washed with water and ethanol to remove the residual oxidant and precipitation on the surface for several times. The obtained sample was dried under vacuum at 40 °C for 12 h and then pyrolyzed under argon at 800 °C, 900 °C and 1000 °C for 2 h. To remove excess metal elements, the pyrolyzed sample was treated with 0.5 M H_2SO_4 solution at room temperature for 12 h and then washed thoroughly with ultrapure water. For comparison, iron free hierarchical porous nitrogen-doped carbon materials (HP–N–Cs) and non-hierarchical porous iron and nitrogen co-doped carbon materials (Fe–N–Cs) were also synthesized. The preparation of HP–N–Cs was the same as described above except for no pre-impregnation step and replacing the $FeCl_3$ oxidant with ammonium persulfate (APS). The non-hierarchical porous sample (Fe–N–Cs) was prepared with PVA hydrogel without polystyrene (PS) colloids as templates under the same preparation processes.

2.3. Characterization

The morphology and microstructure of the samples were investigated by High-transmission electron microscopy (TEM: JEM-2100, operated at 200 kV) and Scanning electron microscopy (FE-SEM: S-4800). X-ray diffraction (XRD) patterns were collected on a powder X-ray diffractometer (RIGAK, D/MAX 2550 VB/PC, Japan). Brunauer–Emmett–Teller (BET) and Barrett–Joyner–Halenda (BJH) models were used to determine the specific surface areas, pore volume, and the pore sizes of the samples, respectively. Raman spectra were recorded with a Bruker RFS 100/S spectrometer. X-ray photoelectron spectroscopy (XPS) was conducted using VG ESCA

2000 with an Mg Kα as source and the C1s peak at 284.6 eV as an internal standard. Electrochemical experiments were conducted on a CHI660C electrochemical workstation (CH Instrument Co., China). A conventional three-electrode system included a glassy carbon rotating disk electrode (RDE) (5 mm in diameter, Pine Research Instrumentation) coated with catalysts, a Pt wire counter electrode and an Ag/AgCl (KCl, 3.5 M) reference electrode. The power density for MFCs was measured by a Source Meter (2400 Keithley, Cleveland, OH).

2.4. Ink and electrode preparation for catalysts

The RDEs were polished with 1 and 0.05 μm alumina slurry sequentially and then washed ultrasonically in ultrapure water and ethanol, respectively. The catalysts (3 mg) were ultrasonically dispersed in the mixed solution of Nafion (5 wt%, 100 μL) and ethanol (900 μL), resulting in a catalyst concentration of 3 mg mL^{-1}. Then the catalyst dispersion (10 μL) was dropped onto the RDE, which yielded a loading of catalyst 0.15 mg cm^{-2}. The resulting electrode was dried under ambient conditions. For MFC cathode fabrication, the catalysts ink was spun-on the 4 cm^2 carbon fiber paper (CFP) substrate with a catalyst loading of 3 mg cm^{-2}.

2.5. Electrochemical measurements

Electrochemical experiments are conducted using CHI660C advanced electrochemical system. A conventional three-electrode cell was employed incorporating a working glass carbon, an Ag/AgCl, KCl (3.5 M) electrode as reference electrode, and a Pt electrode as counter electrode. All potentials were measured and reported vs. the Ag/AgCl, KCl (3.5 M) reference electrode. The electrode is allowed to dry at room temperature before measurement. 100 mM PBS saturated with oxygen served as the supporting electrolyte. The linear sweep voltammograms (LSVs) were recorded in O$_2$ saturated 100 mM PBS with a scan rate of 10 mV s^{-1} at various rotating speeds from 400 to 1600 rpm. After each scan, the electrolyte was saturated with O$_2$ again for 5 min. Koutecky—Levich plots were analyzed at different electrode potentials. The exact kinetic parameters including electron transfer number (n) and kinetic current density (J_K) of the resulting HP—Fe—N—C were analyzed on the basis of the K—L equations [27]:

$$\frac{1}{J} = \frac{1}{J_L} + \frac{1}{J_K} = \frac{1}{B\omega^{1/2}} + \frac{1}{J_K}$$

$$B = 0.2nFC_0(D_0)^{2/3}\nu^{-1/6}$$

In the Koutecky—Levich equations, J, J_L, J_K are the measured current density, the diffusion-limiting current density, and the kinetic-limiting current density, respectively; ω is the rotation speed in rpm, F is the Faraday constant (96485C mol^{-1}), D_0 is the diffusion coefficient of oxygen in 100 mM PBS (2.7×10^{-5} cm^2 s^{-1}), ν is the kinetic viscosity (0.01 cm^2 s^{-1}), and C_0 is the bulk concentration of oxygen (1.2×10^{-6} mol cm^{-3}). 0.2 is a constant when the rotation speed is expressed in rpm.

2.6. MFC construction and operation

The MFC experiments were carried out in a self-made two-chamber H-type MFC which we reported previously [28]. The anode chamber was filled with mixed cultures, carbon granules (diameters of 1—3 mm) and sodium acetate (1000 mg L^{-1}) culture medium solution. The culture medium solution contained: phosphate buffer solution (PBS, 100 mM) and mineral solution (12.5/

1000 v/v) [29]. The catholyte in cathode chamber was 100 mM PBS. Air was purged into the cathode compartment in order to supply the oxygen needed for the electrochemical reaction.

The MFCs were inoculated with a mixture (50/50 v/v) of equalization tank effluent from the sewage treatment plant of the East China University of Science and Technology (Shanghai, China). All tests were conducted at room temperature. The power and current density were normalized by the projected surface area of the cathode (4 cm^{-2}). All tests were conducted in duplicate, and mean values are presented.

3. Results and discussion

Fig. 1 shows the schematic diagram for synthesizing the HP—Fe—N—C composites. In the first step, the composites of PS and PVA hydrogel (PS/PVA) were prepared by a solvent-assisted freeze—thaw method we developed previously, followed by chemical cross-linking to improve their mechanical and chemical stability in good solvents [30]. Afterward, the PVA hydrogel-based composites were used as templates and pre-impregnated into FeCl$_3$ ethanol solution for 5 h at room temperature, producing pale yellow solids (PS/PVA/Fe). Then the PS/PVA/Fe solids were transferred into an ethanol solution of pyrrole monomer and stirred for 30 min. Afterward, an aqueous solution of FeCl$_3$ oxidant was added to the suspension followed by stirring for 24 h at 4 °C, which resulted in black solids (PS/PVA/Fe-PPy). The obtained PS/PVA/Fe-PPy products were allowed to dry at 40 °C for 12 h. Subsequently, the resulting solids were pyrolyzed at 800, 900 and 1000 °C under argon flow and thereby generated the HP—Fe—N—C samples. For simplicity, the samples are denoted as HP—Fe—N—C-800, HP—Fe—N—C-900 and HP—Fe—N—C-1000, respectively. The key feature of our method is the employment of PVA hydrogel. First, for the preparation of PVA/PS hydrogel composite templates, free-standing composite monoliths could be formed by the immobilization of PS colloids within PVA hydrogel through a well-known freeze—thaw process. Moreover, the presence of PVA hydrogel results in improved hydrophilicity of the templates, allowing for a more uniform wetting of the templates during the infiltration process. Finally, and most importantly, the abundant oxygen-containing functional groups on the PVA are favorable for the binding of metal cations and nitrogen. The optical photographs of the free-standing PS/PVA, PS/PVA/Fe and PS/PVA/Fe-PPy monoliths are shown in Fig. S1.

The structure and morphologies of the resulting samples were firstly characterized by field-emission scanning electron microscopy (FE-SEM) measurements. Typical scanning electron microscopy (SEM) image of PVA/PS hydrogel composite templates show that the latex spheres with diameter of ca. 160 nm embedded in the hydrogel are arranged in a close-packed structure (Fig. S2). The inset of Fig. S2 shows that free-standing composite monoliths are formed by utilizing cross-linked PVA hydrogel to stabilize large quantities of polystyrene (PS) colloids. The SEM images for the as-prepared HP—Fe—N—C-900 displayed a specific hierarchical interconnected macroporous structure, as shown in Fig. 2a and b. X-ray diffraction (XRD) was used to obtain structural information about HP—Fe—N—C-900. Fig. 2c shows the X-ray diffraction patterns of the as-prepared HP—Fe—N—C-900. Two sharp peaks at $2\theta = 25°$ and 43°, corresponding to C (002) and (101) diffractions, are observed in the wide-angle XRD pattern, indicating the partially graphitic structure of the nitrogen-doped carbon. No diffraction peaks due to metal or metal oxides are observed in the diffraction patterns, probably due to the low levels of metal. The porous nature of HP—Fe—N—C-900 was accessed with nitrogen adsorption—desorption isotherms (Fig. 2d). The composite shows a type IV isotherms (as defined by IUPAC) with a high BET surface area of
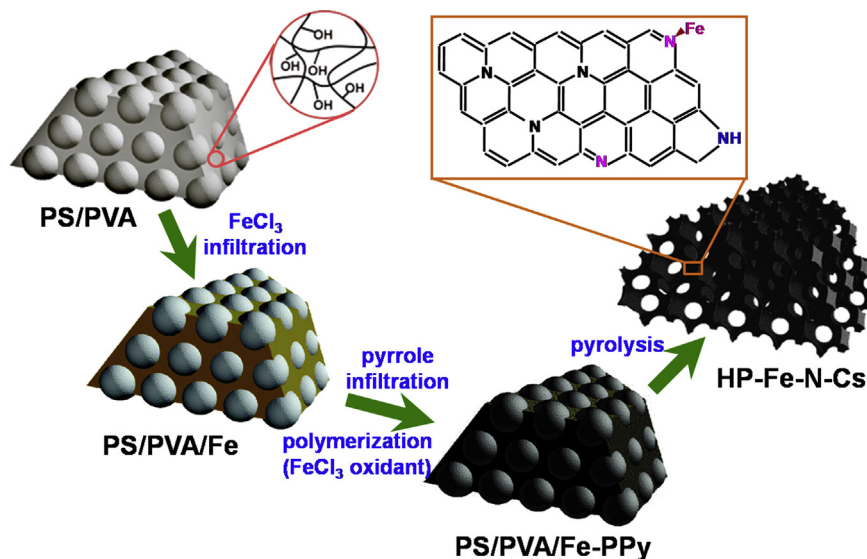
Fig. 1. Schematic diagram of the fabrication process of HP−Fe−N−Cs composites.

506.7 m^2 g^{-1}. The distinct hysteresis loop in the large range of ca. 0.45−1.0P/P_0 indicates the presence of mesoporous structure. The pore size distribution calculated from desorption data using the BJH model, suggests an average value of about 4.41 nm. It is obvious that the high specific surface area is mainly attributed to the formation of a mesoporous structure. The high surface area of the HP−Fe−N−C-900 should provide more surface catalytic sites exposed to oxygen molecules and thus results in ORR activity enhancement. In addition, the mesoporous structure can also provide the possibility of efficient mass transport and thereby lead to enhanced electrocatalytic performance [14,24].

Fig. 3a shows a typical TEM image of the HP−Fe−N−C-900, which further suggests the specific hierarchical interconnected framework and abundant macroporous structure. In addition, a small amount of residual Fe-containing particles with sizes of about 20 nm could also be observed in the carbon layers after the acid leaching treatment (Fig. 3b). High-resolution TEM (HRTEM) revealed the presence of short-range ordered, partially graphitized carbon nanostructure in the carbon layer, as shown in Fig. 3c, which agreed with the XRD results. The carbon structure of HP−Fe−N−C-900 was analyzed by Raman spectra (Fig. 3d). The G-band at 1575 cm^{-1} is associated with the E$_{2g}$ mode of graphitic carbon,
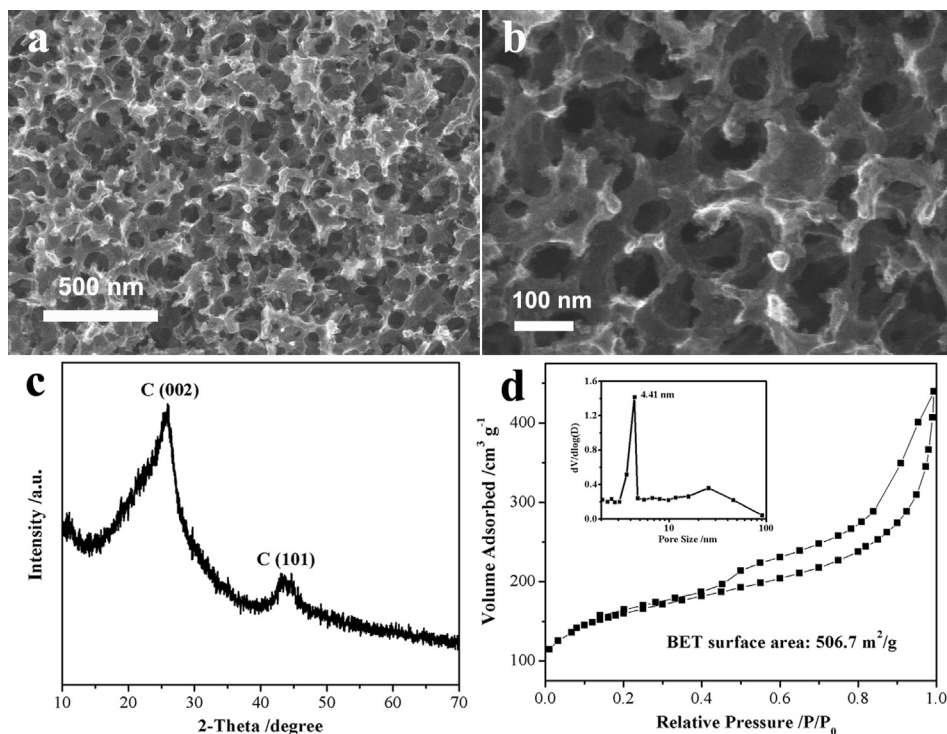

Fig. 2. (a) Low-magnification and (b) high-magnification SEM images of as-prepared HP−Fe−N−C-900 composite. (c) The wide-angle XRD patterns of HP−Fe−N−C-900. (d) N$_2$ adsorption−desorption isotherms and the corresponding pore size distribution (inset) of the HP−Fe−N−C-900.
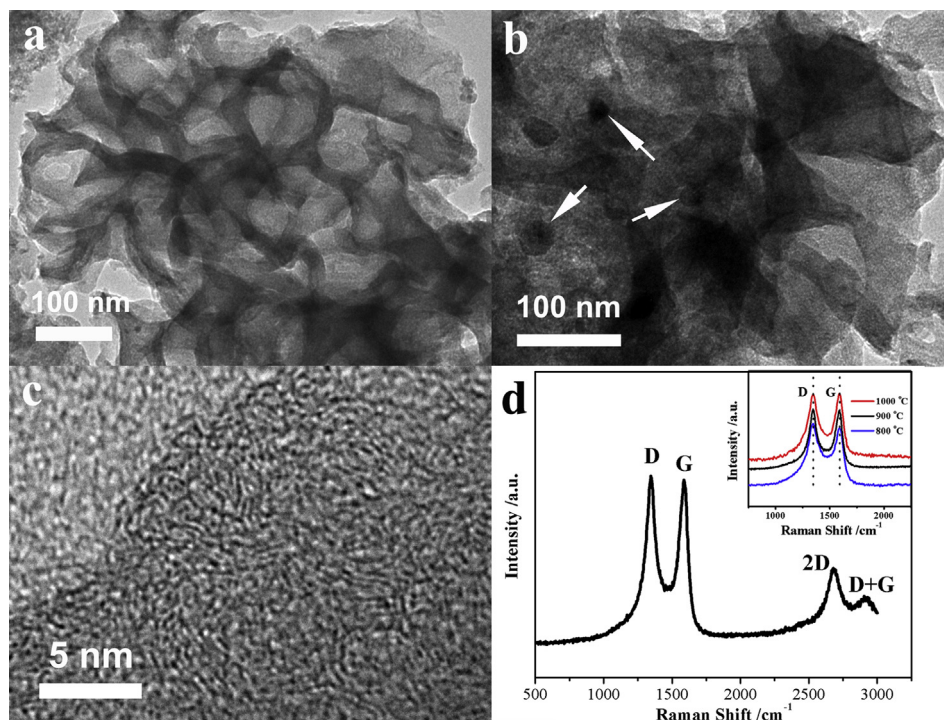
Fig. 3. (a) TEM images of the HP−Fe−N−C-900 composite and (b) the residual Fe-containing nanoparticles, where the white arrows designated. (c) High-resolution TEM image of the carbon layers in the HP−Fe−N−C-900 composite. (d) Raman spectrum of HP−Fe−N−C-900, the inset shows the Raman spectra of the HP−Fe−N−Cs samples pyrolyzed under different temperature.

while the D-band located at 1346 cm^{-1} corresponds to the defect-induced mode, resulting from the possible amorphous carbon with heteroatoms doping in HP−Fe−N−C-900. The broad bands centered at 2680 cm^{-1} and 2900 cm^{-1} are ascribed to the 2D and D + G bands. The inset of Fig. 3d shows the Raman spectra of HP−Fe−N−Cs samples pyrolyzed under different temperatures, the I_G/I_D ratio increases as the pyrolysis temperature increases from 800 to 1000 °C, suggesting enhanced graphitization of carbons at higher temperature.

XPS of the HP−Fe−N−C-900 provided further evidence for the incorporation of Fe and N into the carbon. As shown in Fig. 4a and part (a) of Table S1, the atomic ratios of N (N 1s in Fig. 4c), O (O1s in Fig. 4e), and Fe (Fe 2p in Fig. 4f) relative to C of the HP−Fe−N−C-900 sample were ∼0.042, 0.107, and 0.004, respectively. The high-resolution C 1s spectrum (Fig. 4b) showed that there were C=C, C=N & C−O, C−N & C=O and O−C=O components, and the N 1s peak can be deconvoluted into three components: pyridinic N and Fe−N$_x$ (398 eV), pyrrolic N (400 eV), and graphitic N (401 eV), these results suggested the successful incorporation of nitrogen atoms within the graphitic structure of HP−Fe−N−C-900. The percentage compositions of each N species from N 1s were listed in part (b) of Table S1, which demonstrates a highest content of graphitic N (48.4%) and a high fraction of pyridinic N (32.6%). It has been demonstrated that graphitic N could greatly increase the limiting current density, and pyridinic N could improve the onset potential, while other N species such as pyrrolic N had little effect on the electrochemical performance of carbon materials [13]. Furthermore, some previous work have reported that a larger amount of graphitic N than pyridinic N is considered to be more favorable for ORR [31,32]. Then, it could be anticipated that the HP−Fe−N−C-900 we prepared here might have a high catalytic activity for ORR. The high-resolution O 1s spectrum could be fitted into three peaks at 533.1, 532.0, and 531.0 eV, which corresponds to hydroxyls, carboxyls and physically adsorbed oxygen/carbonates, respectively

[33]. It should be noted that the signal of Fe was too weak to determine the Fe valence state. However, because pyridinic N can coordinate with Fe, then based on the high percentage of the pyridinic N species in our XPS finding, it could be inferred that Fe−N$_x$ bonds might be formed in HP−Fe−N−C-900 [21,34]. We believe that the formation of Fe−N$_x$ bonds together with C−N bonds both play crucial roles in promoting the ORR catalytic performance.

To study the effect of the pyrolysis temperature on the catalytic activities of HP−Fe−N−Cs, linear-sweep voltammograms at 1600 rpm were collected in O$_2$-saturated 0.1 M PBS for HP−Fe−N−C samples carbonized under different temperatures. In order to minimize the effect of residual currents on the potential value, the onset potential in this research has been defined as a potential required for generating an ORR current density of 0.1 mA cm^{-2} in the LSV experiments. As shown in Fig. 5a, the HP−Fe−N−C-900 demonstrated an ORR onset potential of 0.197 V, which is more positive than those of HP−Fe−N−C-800 (0.149 V) and HP−Fe−N−C-1000 (0.176 V). Also the limiting current density of HP−Fe−N−C-900 was 5.44 mA cm^{-2} at −0.5 V, which is substantially higher than those of HP−Fe−N−C-800 (3.91 mA cm^{-2}) and HP−Fe−N−C-1000 (4.60 mA cm^{-2}). Furthermore, compared with the commercial Pt/C catalyst, the onset potential for HP−Fe−N−C-900 was close to that of Pt/C (0.272 V), and the current density for HP−Fe−N−C-900 at −0.5 V is even a little bit higher than that of Pt/C (5.32 mA cm^{-2}), indicating a competitive ORR catalytic activity of HP−Fe−N−C-900 to Pt/C in neutral media. Typical LSVs of HP−Fe−N−C-900 at various rotating speeds were also recorded. As shown in Fig. 5b, the voltammetric profiles for HP−Fe−N−C-900 in O$_2$-saturated 0.1 M PBS electrolyte indicated that the current density was enhanced with increasing rotation rates (from 400 to 1600 rpm). The corresponding Koutecky−Levich plots (J^{-1} vs W$^{-1/2}$) at different electrode potentials for HP−Fe−N−C-900 exhibit good linearity and parallelism, implying first order reaction kinetics with respect to the dissolved O$_2$ (Fig. 5c). The inset of Fig. 5c demonstrates that the
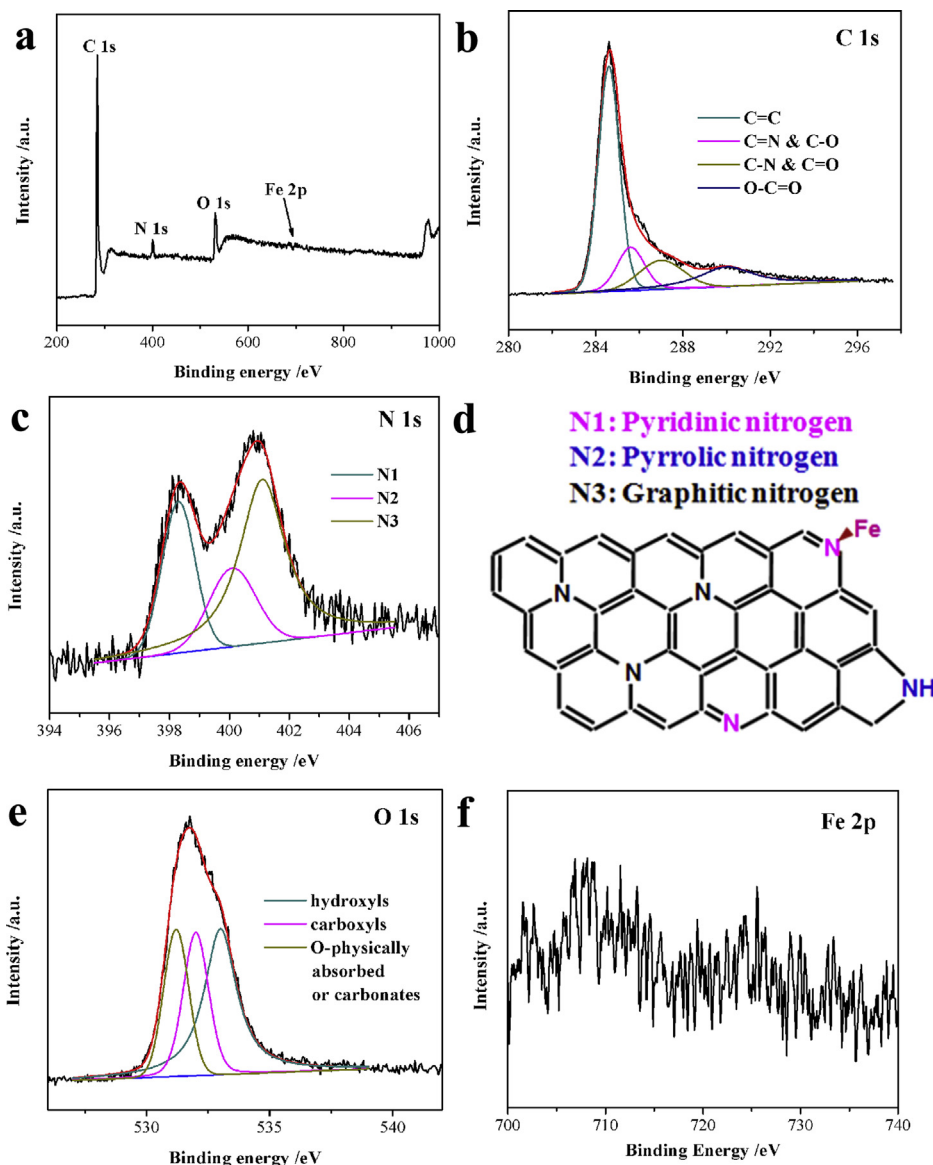
Fig. 4. (a) The wide XPS survey of HP−Fe−N−C-900. The high resolution (b) C 1s, (c) N 1s, (e) O 1s and (f) Fe 2p spectra. (d) Schematic structure of the predicted bonding configurations of N atoms in HP−Fe−N−C-900.

electron transfer number of HP−Fe−N−C-900 remains approximately constant at 3.86 over the potential range from −0.40 to −0.60 V, emphasizing the ORR process proceeds mainly via a four-electron mechanism. Fig. 5d showed the Koutecky−Levich plots for HP−Fe−N−C samples carbonized under different temperatures at −0.50 V, the corresponding electron transfer numbers calculated based on the Koutecky−Levich equation were also listed in Fig. 5d. The higher electron transfer number of HP−Fe−N−C-900 than those of HP−Fe−N−C-800 (3.48) and HP−Fe−N−C-1000 (3.69) further confirmed the best ORR activity acquired under the pyrolysis temperature of 900 °C. Similarly, the ORR kinetics on Pt/C electrode were also analyzed, which shows a slightly higher electron transfer number of 3.98 at −0.50 V than HP−Fe−N−C-900, indicating a more efficient ORR process than HP−Fe−N−C-900.

To better compare and understand the ORR performance of the HP−Fe−N−Cs samples, iron-free hierarchical porous nitrogen-doped carbon (HP−N−C) and non-hierarchical porous samples (Fe−N−C) were also prepared. The HP−N−C composite shows a similar morphology to the HP−Fe−N−C, with an interconnected macroporous structure. However, a non-interconnected macroporous structure was observed for the Fe−N−C sample due to the absence of polystyrene (PS) colloids. The ORR performances of HP−N−C and Fe−N−C were also tested in O_2-saturated 0.1 M PBS and compared with HP−Fe−N−C-900 composite. As shown in Fig. 6a, the Fe−N−C (0.164 V and 4.04 mA cm^{-2}) shows obviously better ORR activity than the HP−N−C (0.028 V and 2.69 mA cm^{-2}), implying the better performance brought about by the introduction of Fe (Fe−N$_x$ moieties) than the hierarchical porous structure. Meanwhile, although the Fe−N−C shows an onset potential close to that of HP−Fe−N−C-900, the current density of Fe−N−C at −0.50 V is much lower than that of HP−Fe−N−C-900, which suggests an enhanced surface density of catalytic sites (Fe−N$_x$ moieties) presented onto the hierarchical porous structure of the HP−Fe−N−C-900 composite. To get insight into the kinetic differences in ORR catalysis on HP−N−C, Fe−N−C and HP−Fe−N−C-900, the Koutecky−Levich plots at −0.50 V for the three samples were shown in Fig. 6b, the corresponding electron transfer number and kinetic current density (J_k) calculated based on the Koutecky−Levich
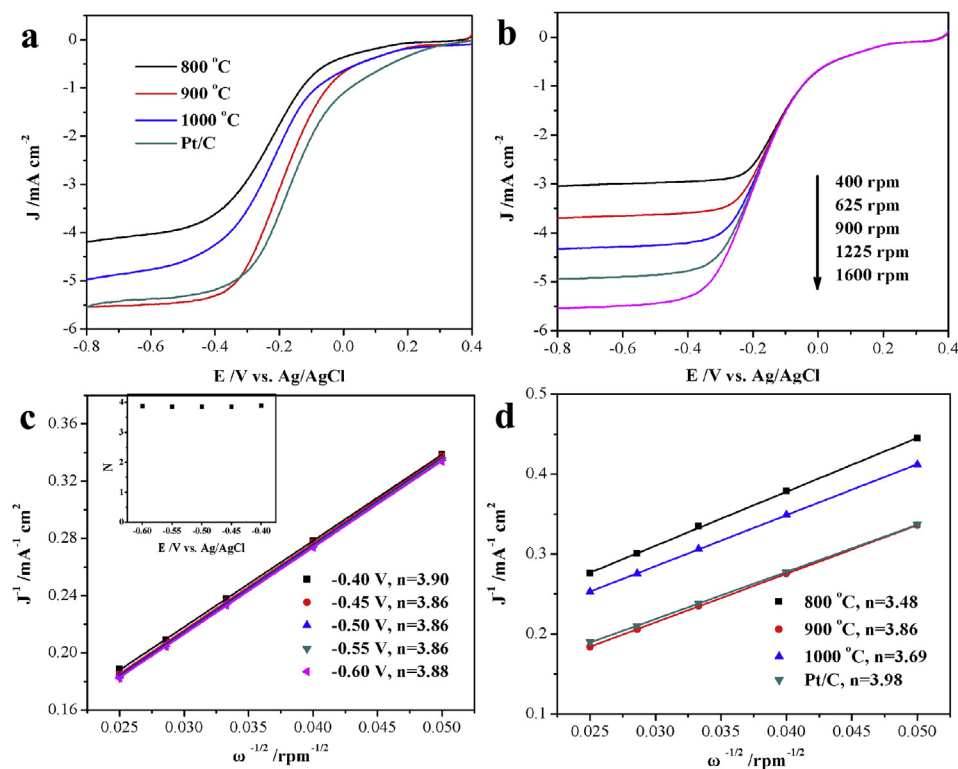
Fig. 5. (a) Linear sweep voltammograms of the HP–Fe–N–Cs samples and Pt/C at a rotation rate of 1600 rpm. (b) Typical LSVs at different rotating speeds in an O₂-saturated 0.1 M PBS solution at a scan rate of 10 mV s⁻¹ and (c) the corresponding K–L plots for HP–Fe–N–C-900, the inset of (c) shows the electron transfer number at different potentials. (d) K–L plots at −0.5 V for the HP–Fe–N–Cs samples and Pt/C.
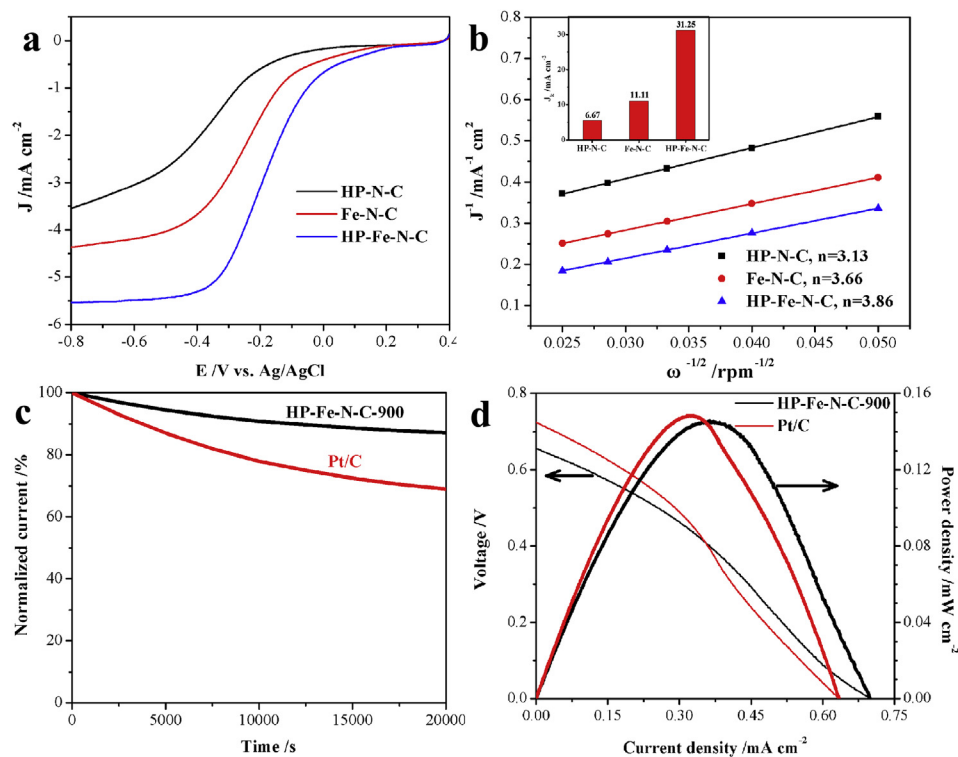

Fig. 6. (a) Linear sweep voltammograms of HP–Fe–N–C–900, Fe–N–C and HP–N–C samples at a rotation rate of 1600 rpm. (b) K–L plots at −0.5 V for HP–Fe–N–C-900, Fe–N–C and HP-N-C samples, inset show the corresponding J_k values. (c) I–t plots of HP–Fe–N–C-900 and Pt/C at −0.4 V in O₂-saturated 0.1 M PBS solution. (d) Polarization curves (thin line) and power density curves (bold line) of MFCs with cathode catalysts of HP–Fe–N–C-900 and Pt/C (Catalysts loading: 3 mg cm⁻², normalized to the cathode surface area).

equation were also listed and depicted in the inset of Fig. 6b. The higher electron transfer number and J_k of HP−Fe−N−C-900 than those of HP−N−C and Fe−N−C further manifest that a synergetic promotion of ORR performance arises from the combination of Fe (Fe−N$_x$ moieties) incorporation and the hierarchical porous structure.

In addition to the activity, the stability is another key parameter for high-performance electrocatalysts. We conducted a 20,000 s stability test for HP−Fe−N−C-900 toward ORR by chronoamperometry at a constant voltage of −0.4 V in O$_2$-saturated 0.1 M PBS solution at a rotation rate of 1600 rpm. As seen in Fig. 6c, although the current densities of both HP−Fe−N−C-900 and commercial 20% Pt/C decrease with time, the HP−Fe−N−C-900 exhibits a very slow attenuation and a high relative current of 87.2% still persists after 20,000 s, while only 69.2% of the initial catalytic current is kept for 20% Pt/C catalyst in the same testing time. This result demonstrates that the HP−Fe−N−C-900 holds better duration stability than commercial 20% Pt/C for ORR in neutral media.

The ORR electrocatalysts should also be robust in the real application. To study the possibility of using HP−Fe−N−C-900 as an alternative to Pt/C and evaluate the ORR performance of HP−Fe−N−C-900 cathode catalyst in practical applications in biological systems, we set up a home-made mixed bacteria inoculated H-shaped aqueous cathode MFC which we reported previously and examined the MFC performances equipped with HP−Fe−N−C-900 and Pt/C as cathode catalysts. As shown in Fig. 6d, the open circuit voltage for HP−Fe−N−C-900 composite was 0.66 ± 0.01 V, which is slightly lower than the commercial Pt/C catalyst (0.72 ± 0.01 V). However, the short-circuit current density of HP−Fe−N−C-900-MFC (0.69 ± 0.02 mA cm^{-2}) is higher than that of Pt/C-MFC (0.63 ± 0.02 mA cm^{-2}), which could be due to the efficient mass transfer arised from the hierarchical porous structure of HP−Fe−N−C-900. As a result, the HP−Fe−N−C-900-MFC achieved a maximum power density of 0.14 ± 0.01 mW cm^{-2} which is comparable to that of Pt/C-MFC (0.15 ± 0.01 mW cm^{-2}). These results suggest that, using HP−Fe−N−C-900 composite as cathodic catalyst in the practical biological systems, the oxygen reduction reaction happened in the cathode can be efficient and comparable to the commercial Pt catalyst. In addition, the hierarchical porous structure of the HP−Fe−N−C-900 catalyst could also provide multidimensional transport pathways, reduce the diffusion effect and promote the interfacial transport for the ORR-relevant species (H$^+$, OH$^-$, e$^-$, O$_2$, H$_2$O). Therefore, the HP−Fe−N−C-900 composite can be anticipated to replace the expensive Pt/C as a promising cathode catalyst.

4. Conclusions

In summary, hierarchical porous iron and nitrogen co-doped carbons (HP−Fe−N−Cs) were prepared by using polypyrrole as nitrogen source and poly(vinyl alcohol) (PVA) hydrogel-based composites as in-situ templates. The HP−Fe−N−C-900 composite shows efficient ORR catalytic activity and superior stability than the commercial Pt/C catalyst in neutral media, which could be due to the combination of the abundant ORR active sites probably from the Fe−N$_x$ and C−N bonds and the efficient mass transfer from the hierarchical porous structure. Furthermore, microbial fuel cells (MFCs) equipped with HP−Fe−N−C-900 catalyst on cathodes exhibits comparable power outputs than that of MFCs with the commercial Pt/C cathode catalysts. It could be anticipated that the HP−Fe−N−Cs with the unique hierarchical porous architectures

would offer a competitive advantage over state-of-the-art Pt/C catalysts and become a promising cathode catalyst candidate for a new generation of low-cost and high-performance fuel cells.

Appendix A. Supplementary data

Supplementary data related to this article can be found at http://dx.doi.org/10.1016/j.jpowsour.2014.04.140.

References

[1] D. Wang, H.L. Xin, R. Hovden, H. Wang, Y. Yu, D.A. Muller, F.J. DiSalvo, H.D. Abruña, Nat. Mater. 12 (2013) 81–87.
[2] Y. Liang, Y. Li, H. Wang, J. Zhou, J. Wang, T. Regier, H. Dai, Nat. Mater. 10 (2011) 780–786.
[3] Y. Bing, H. Liu, L. Zhang, D. Ghosh, J. Zhang, Chem. Soc. Rev. 39 (2010) 2184–2202.
[4] J. Wu, H. Yang, Acc. Chem. Res. 46 (2013) 1848–1857.
[5] Y. Tan, C. Xu, G. Chen, X. Fang, N. Zheng, Q. Xie, Adv. Funct. Mater. 22 (2012) 4584–4591.
[6] J. Yang, X. Chen, X. Yang, J.Y. Ying, Energy Environ. Sci. 5 (2012) 8976–8981.
[7] Z. Yang, H. Nie, X.a. Chen, X. Chen, S. Huang, J. Power Sources 236 (2013) 238–249.
[8] Y. Zheng, Y. Jiao, M. Jaroniec, Y. Jin, S.Z. Qiao, Small 8 (2012) 3550–3566.
[9] K. Gong, F. Du, Z. Xia, M. Durstock, L. Dai, Science 323 (2009) 760–764.
[10] P. Chen, T.-Y. Xiao, Y.-H. Qian, S.-S. Li, S.-H. Yu, Adv. Mater. 25 (2013) 3192–3196.
[11] D. Geng, Y. Chen, Y. Chen, Y. Li, R. Li, X. Sun, S. Ye, S. Knights, Energy Environ. Sci. 4 (2011) 760–764.
[12] R. Liu, D. Wu, X. Feng, K. Müllen, Angew. Chem. Int. Ed. 49 (2010) 2565–2569.
[13] L. Lai, J.R. Potts, D. Zhan, L. Wang, C.K. Poh, C. Tang, H. Gong, Z. Shen, J. Lin, R.S. Ruoff, Energy Environ. Sci. 5 (2012) 7936–7942.
[14] W. Yang, T.-P. Fellinger, M. Antonietti, J. Am. Chem. Soc. 133 (2010) 206–209.
[15] H. Liu, Z. Shi, J. Zhang, L. Zhang, J. Zhang, J. Mater. Chem. 19 (2009) 468–470.
[16] Z. Liu, H. Nie, Z. Yang, J. Zhang, Z. Jin, Y. Lu, Z. Xiao, S. Huang, Nanoscale 5 (2013) 3283–3288.
[17] R. Silva, D. Voiry, M. Chhowalla, T. Asefa, J. Am. Chem. Soc. 135 (2013) 7823–7826.
[18] J. Liang, Y. Zheng, J. Chen, J. Liu, D. Hulicova-Jurcakova, M. Jaroniec, S.Z. Qiao, Angew. Chem. Int. Ed. 51 (2012) 3892–3896.
[19] G. Wu, P. Zelenay, Acc. Chem. Res. 46 (2013) 1878–1889.
[20] H.-S. Oh, H. Kim, J. Power Sources 212 (2012) 220–225.
[21] M. Lefevre, E. Proietti, F. Jaouen, J.P. Dodelet, Science 324 (2009) 71–74.
[22] G. Wu, K.L. More, C.M. Johnston, P. Zelenay, Science 332 (2011) 443–447.
[23] H. Jiang, Y. Su, Y. Zhu, J. Shen, X. Yang, Q. Feng, C. Li, J. Mater. Chem. A 1 (2013) 12074–12081.
[24] H.-W. Liang, W. Wei, Z.-S. Wu, X. Feng, K. Müllen, J. Am. Chem. Soc. 135 (2013) 16002–16005.
[25] D.-W. Wang, F. Li, M. Liu, G.Q. Lu, H.-M. Cheng, Angew. Chem. Int. Ed. 47 (2008) 373–376.
[26] H. Jiang, X. Yang, C. Chen, Y. Zhu, C. Li, New J. Chem. 37 (2013) 1578–1583.
[27] A.J. Bard, L.R. Faulkner, Electrochemical Methods: Fundamentals, Application, second ed., John Wiley & Sons, Inc., New York, 2001, p. 341.
[28] Y. Su, Y. Zhu, X. Yang, J. Shen, J. Lu, X. Zhang, J. Chen, C. Li, Ind. Eng. Chem. Res. 52 (2013) 6076–6082.
[29] D.R. Lovley, E.J.P. Phillips, Appl. Environ. Microbiol. 54 (1988) 1472–1480.
[30] H.K. Purss, G.G. Qiao, D.H. Solomon, J. Appl. Polym. Sci. 96 (2005) 780–792.
[31] B. Zheng, J. Wang, F.-B. Wang, X.-H. Xia, Electrochem. Commun. 28 (2013) 24–26.
[32] H. Niwa, K. Horiba, Y. Harada, M. Oshima, T. Ikeda, K. Terakura, J.-i. Ozaki, S. Miyata, J. Power Sources 187 (2009) 93–97.
[33] V. Datsyuk, M. Kalyva, K. Papagelis, J. Parthenios, D. Tasis, A. Siokou, I. Kallitsis, C. Galiotis, Carbon 46 (2008) 833–840.
[34] F. Charreteur, F. Jaouen, S. Ruggeri, J.-P. Dodelet, Electrochim. Acta 53 (2008) 2925–2938.